Transactions of the Nigerian Association of Mathematical Physics
Volume 14, (January - March, 2021 Issue), pp187 –194

STRUCTURAL AND DIELECTRIC STUDY OF SR^{2+} SUBSTITUTED BARIUM HEXAFERRITE

[1]Y. Abdu and [2]I. M. Musa

[1]Department of Physics, Bayero University, Kano. Nigeria.
[2]Department of Physics, Federal University Dutse, Jigawa State. Nigeria.

Abstract

The synthesis of Sr^{2+} substituted M-type Barium nanohexaferrites with $Ba_{1-x}Sr_{0.2}Fe_{12}O_{19}$ (x= 0.20, and 0.7) chemical compositions was successfully carried out via sol-gel auto-combustion technique. The formation of single phase hexagonal ferrites with presence of hematite phase was confirmed from XRD spectra which diminish with the substitution. the cystallites sizes were in the range of 26.40nm-29.91nm, the lattice constants were found to decrease with increase in ions substitutions. The FTIR spectra of the sample show three dominants peaks in the range 400-600 cm^{-1} which indicate the formation of the desired hexaferrites structure. The dielectric properties typical of hexaferrites with low dielectric loss was confirmed on all the samples which decreases with the substitution. The dielectric constant was enhanced at high frequency in the entire sample and reduction of dielectric loss was also observed which was dependent on ions substitutions. The grain boundary resistance contributes most to the dielectric properties as indicated by the Nyquist plot, whereas the AC conductivity is the dominant conducting mechanism in the material which was found to decrease with increase in ions substitutions. The properties of the synthesized material could be useful for applications in electronics and high frequency absorbing devices.

***Keywords*:** M-type nano-hexaferrites, sol-gel auto-combustion, metal ions substitutions, materials properties.

1.0 Introductıon

Hexagonal ferrites have witnessed an increasing exploration since their discovery in 1950 by Philips laboratory. This was as a result of their excellent magnetic properties with coercivity (Hc) of 6700 Oe, saturation magnetization (Ms) of 72 emu/g and Curie temperature (Tc) of 502 °C[1]. This excellent magnetic properties make them suitable for application in magnetic storage and recording media, electronic components operating at microwave (MW) and gigahertz (GHz) frequency, magnetoelctric and multiferroic application, radar absorbing material (RAM), aircraft (stealth technology), low-power spintronics devices, circulators and phase shifters [2,3]. Hexagonal ferrites are divided into six types according to their chemical composition and crystalline structure; M-type($BaFe_{12}O_{19}$), Y-type($Ba_2Me_2Fe_{12}O_{22}$), U-type($Ba_4Me_2Fe_{36}O_{60}$), W-type($Ba_2Me_2Fe_{16}O_{27}$), X-type($Ba_2Me_2Fe_{28}O_{46}$), and Z-type($Ba_3Me_2Fe_{24}O_{41}$). The symbol Me_2 in the chemical formular stands for low divalent ion mainly zinc, cobalt, magnesium, nickel and strontium [4, 5]. M-type hexagonal ferrites possess magnetoplumbite structure and belong to the space group P63/mmc. The structure of M-type hexagonal ferrites is a superposition of R and S blocks along the hexagonal c-axis with stacking sequence describing the unit cell as RSR*S*. The letter R represents a block of three layers of oxygen ions (O_4-BaO_3-O_4) with composition $BaFe_6O_{11}$ and S is a spinel block of two layers of oxygen ions with composition (O_4-O_4). The asterisk indicate that the corresponding block is rotated 180° around the hexagonal c-axis. There are 38 O^{2-} ions, 2 Ba^{2+} ions, 24 Fe^{3+} ions in a unit cell of hexagonal ferrite. However, the Fe^{3+} ions occupy five sites in the structure which are trigonal bi-pyramidal site (2b), tetrahedral site (4f1) and octahedral

Correspondence Author: Abdu Y., Email: ayunusa.phy@buk.edu.ng, Tel: +2348029174511

sites (12 k, 2a and 4f2). Two out of the five sites (4f1 and 4f2) have spin-down ferric ions which cause reduction in average magnetic moment of the molecule. In order to enhance the magnetic and dielectric properties of the hexagonal ferrites, appropriate cations with spin up such as rare-earth or transition metals are substituted at spin-down site. Single, two or even more cations can be substituted, but electronegativity must be maintain. Amongst all the different types of hexaferrites, M-type hexagonal ferrites show better performance compared to others. The performance in which they excelled includes high curie temperature, moderate energy product, large coercivity, strong uniaxial anisotropy, high saturation magnetization, high remanant magnetization. Besides, it can easily be produced by low temperature sytheses without formation of magnetite (Fe_2O_3) as secondary phase[6, 7]. It was reported by various researchers that the electrical, optical and magnetic properties of ferrites are very sensitive to particle size, shape and degree of crystallinity which are attributed to synthesis techniques and nature of the substituted cations [8 - 12], Sol-gel autocombustion method was reported to be more effective, as it ensures the formation of single phase at low temperature, via utilisation of heat given off during oxidation process, thereby reducing the formation temperatue[13-15]. This technique has been used to synthesize $Sr_{1-x}Pr_xFe_{12-y}Co_yO_{19}$ (x=0.0,0.2,0.4 y=0, 0.15,0.35) and recorded a decrease in bandgap energy and a characteristic absorption coefficient of 40dB at 18GHz [16]. In a related report by the same researchers, this technique was also used to produced $Sr_{1-x}Cu_{x}Fe_{12-y}Er_yO_{19}$ (x=0.0,0.1,0.2 y=0, 0.4,0.5) and obtained an increase in band gap with subtitution of Er^{+3}. The substitution of Er^{+3} caused spin canting effect and collapse of magnetic collinearity. This results in a decrease in M_s and Cu^{+2} which influenced magnetocrystalline anisotropy in the negative manner leading to decrease in H_c [16]. Another literature reported a particle size of 22.91nm and anhencement in the dielectric properties at higher frequency in $Ba_{1-x}Dy_xFe_{12-y}Cr_yO_{19}$ (x=0.0,0.1,0.2 y=0.0, 0.4, 0.5) [17]. Reduction in coercivity with increase in magnetization of $Sr_{0.5}Ca_{0.5}Fe_{12}O_{19}$ prepared using conventional solid state method was also reported [15]. The sol-gel method was used in the preparation of $Ba_{1-x}Ce_xFe_{12}O_{19}$ (x=0.0,0.05,0.1,0.2) and the results showed an average particle size of 500nm. In addition, it was however observed that M_s initially increased and then later decreased. Then H_c, even though showing no reaction with ions substitution had a value of 5088Oe. The value of Ms and absorption coefficient were found to be 53em/g and 20.47dB, with absorption capacity of up to 16.22GHz [24]. Moreover, substitutions of transition, rare earth elements (RE) and post transition metals ions in Ba^{+2} or Fe^{+3} sites led to a large change in the electromagnetic properties. Meanwhile, RE cations are known to have grain growth inhibition behaviour, this result in enhancement of electromagnetic and optical properties. Typically, the substitution of Gd-Co, Cr-Zn, Ca , Sc or In for Fe reduces H_A and substitution of Al and Ga leads to increase in H_A [18-20]. In this research work, electromagnetic and dielectric properties of hexaferrites material are enhanced by introducing more than one dopant (co-doping). This was acheived through the substitution of Ba^{+2} and Fe^{+3} ions with some amount of M ions using sol-gel Autocombustion technique. The effects of substituted cations on particle size, Morphological, diectric and structural properties of the material were investigated.

2.0 Materıals and Synthesis

The chemicals used for the synthesis of $Ba_{1-x}Sr_xFe_{12}O_{19}$ (x= 0.20, and 0.7) were obtained from LOBA Chemie. These include barium nitrate ($Ba(NO_3)_2$), strontium nitrate ($Sr(NO_3)_2$), ferric nitrate ($Fe(NO_3)_3.9H_2O$), and citric acid ($C_6H_8O_7$). The salt solution was produced via the dissolution of weighted metal salts in ethylene glycol at room temperature. Citric acid was added to the salt solution keeping the molar ratio of citric acid and the metal nitrates at 1:1.5. the pH was then adjusted to 7.00 by adding Ammonia solution in dropwise in order not to exceed the required pH. The solution was then heated for about 3hours with magnetic heating stirrer at 80-100^{o}C to evaporate the ethylene glycol and to obtain a brown gel viscous solution. The solution was later heated at 280-300 ^{o}C for 30 minutes and the gel turned to fluffy precursor powder. There was also the occurrence of auto-combustion accompanied by the release of volatile gases of NH_3, HNCO, and N_2. The materials were finally calcinated at 1100^{o}C for 6 hours to obtain the desired hexagonal phase.

3.0 Characterization Techniques

The x-ray diffractometer (XRD) (Bruker AXSD8 advance diffractometer) was used to study the structure of the synthesized M-type hexaferrites. XRD patterns were recorded between 20°–80° range. Fourier transform infrared (FTIR) spectrometer (Nicolet FTIR interferometer IR prestige-21(model-8400S)) was used to study the nature of the attached functional groups of the material. The study of the morphology of the samples was done using FESEM, MIRA3 TESCAN, USA instrument. The FESEM was operated at 5mm working distance with 5 to 10kV accelerating voltage.

Impedance analyzer (Wayne Kerr 6500B) having 0 to +40V DC bias voltage and 0 to 100mA DC bias Current was used in calculating all dielectric parameters (dielectric constant, dissipation factor and AC conductivity). However, the impedance spectra were recorded via passing radiation through a 9mm thickness pellet prepared by coating with silver conducting paint, to make them suitable for use in the measuring instrument.

4.0 Results and Dıscussıon

The results and discussion are presented in the following order: the XRD analysis, FTIR analysis, FESEM analysis, RAMAN spectroscopy and the Dielectric analysis.

XRD Analysis

The x-ray diffractometer (XRD) (Bruker AXSD8 advance diffractometer) was used to study the structure of the synthesized M-type hexaferrites. XRD patterns were recorded between 20°–80° range. The XRD spectra of $Ba_{1-x}Sr_xFe_{12}O_{19}$ (x= 0.20, and 0.7) are shown in Figure 1. The diffraction peaks were indexed using JCPDS card no. 39–1433. The XRD peaks shows the existance of M-type magnetoplumbhite hexagonal structure. The observed α-Fe_2O_3(JCPDS 00033664), in the XRD spectra show the presence of some trace of hematite phase, this phase decreses immensily with increase in Sr^{2+} concentration. The c/a ratio of all the samples is not greater than 3.98 as shown in table 2, this implies that all the samples exhibit hexagonal structure, due to the fact that hexaferrite materials can be regarded as having hexagonal structure when c/a ratio of the material is not greater than 3.98 [5]. The values of the lattice parameters for all the samples are shown in Table 2. These values have slightly decreased with the substitution. As the concentration of dopant increased, the value of 'c' and 'a' decreased.

The values of the crystallites size obtained in the range 26.40nm –29.91, Table 1. The average crystallite size are 29.91, and 26.40nm, for $Ba_{0.8}Sr_{0.2}Fe_{12}O_{19}$ and $Ba_{0.3}Sr_{0.7}Fe_{12}O_{19}$ respectively, with 29.91nm as maximum size obtained. The crystallite size was decreasing instead of increasing with substitution this arises as a result of the strain produced in the unit cell. Moreover, XRD spectra have broadening of characteristic peaks of the full width at half maxima which is attributed to the crystallite size reduction [20]. Furthermore, the improvement towards hexagonal structure occurs as a result of variation of the strain with elemental substitution which occurs during synthesis and calcination processes.[20]

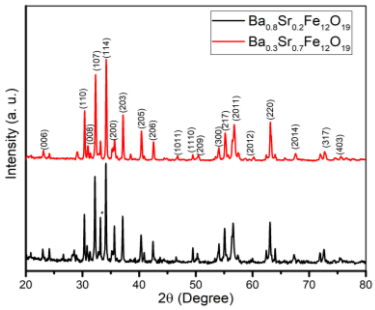

Figure 1. XRD spectra of $Ba_{1-x}Sr_xFe_{12}O_{19}$ (x= 0.20, and 0.7)

Table 1 Calculated sample lattice constants, from XRD result

Sample Code	2θ(°)	d(Å)	β(°)	a(Å)	c(Å)	V(Å^3)	c/a	D(Å)
$Ba_{0.8}Sr_{0.2}Fe_{12}O_{19}$	30.202	2.95675	0.272	5.9135	23.25008	704.5833	3.931695	299.1468
$Ba_{0.3}Sr_{0.7}Fe_{12}O_{19}$	30.202	2.9567	0.308	5.9135	23.2806	705.50	3.936	264.18

FTIR Analysis

The spectra were recorded at room temperature in the wavenumber range 4000cm^{-1} and 400cm^{-1}. The FTIR spectra of $Ba_{1-x}Sr_xFe_{12}O_{19}$ (x= 0.20, and 0.7) is shown in Figure 2. The characteristics bands appears between 400-600 cm^{-1} on each spectrum, mainly at 589cm^{-1},535cm^{-1} and 425cm^{-1}. These are prominant peaks corresponding to a symmetric stretching and out of plane vibrations of metal oxide (Fe-O) in octahedral and tetrahedral sites which indicate the formation of hexaferrites[21]. The 775cm^{-1} peak stand for O-Fe-O vibration mode [17]. The observed band at 1551 cm^{-1} indicated the occurance of metal-oxygen-metal (M-O-M), mainly iron-oxygen-iron vibrational modes[16]. An intense bands around 2060 cm^{-1} and 2368 cm^{-1} are identified to be the O-C-O stretching bands [17]. The peak at 3736 cm^{-1} reveals the vibration of hydroxyl group in the sample which is attributed to bending mode of H-O-H [19].

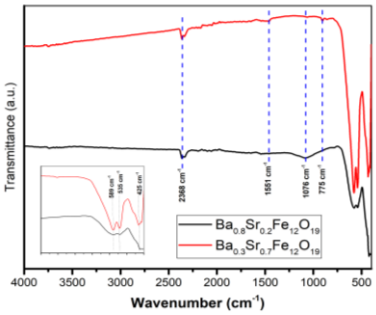

Figure 2. FTIR spectra of $Ba_{1-x}SrxFe_{12}O_{19}$ (x= 0.20, and 0.7)

FESEM Analysis

The FESEM micrographs of $Ba_{1-x}Sr_xFe_{12}O_{19}$ (x= 0.20, and 0.7) are shown in Figure 3. The micrographs show that the sample possessed hexagonal platelet-like structure. The average grain size changes with the introduction of dopants as seen in figure 3a and b. The average grain size obtained using ImageJ processing software for the two samples in the micrographs are 0.1027µm and 0.0350µm, respectively. There also exist a magnetic interaction between the particles which caused agglomeration and non-uniform distribution of grains.

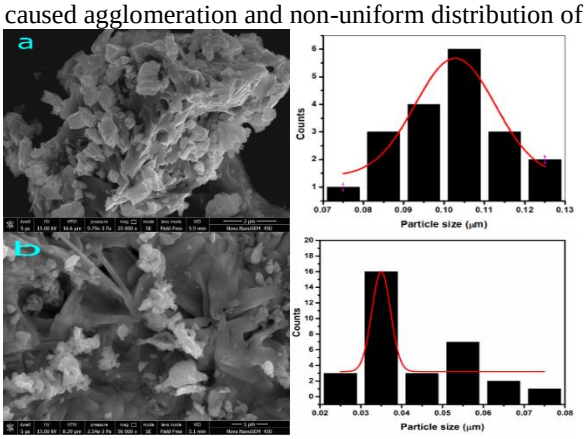

Figure 3. FESEM micrographs of $Ba_{1-x}Sr_xFe_{12}O_{19}$ (x= 0.20, and 0.7)

RAMAN Spectroscopy

The Raman analysis of $Ba_{1-x}Sr_xFe_{12}O_{19}$ (x= 0.20, and 0.7) was carried out and the results are shown in Figure 4. The Raman spectra show a combination of weak and intense Raman active modes at 177, 224, 292, 328, 413, 465, 526, 613, and 684 cm^{-1}. These values agreed with the characteristic bands of pure M-type hexaferrites. The observed bands was assigned to various vibrational modes based on comparisons with reference data, Table 2 [21-25]. The obseved peaks 177 and 224 cm^{-1} appearing at lower Raman shift, correspond to whole spinel block vibrational mode due to E_{1g} symmetry [21]. The mode at 224 cm^{-1} was extremely weak in the sample MA1. A moderately intense peak at 328 cm^{-1} corresponds to octahedral 12k site vibration due to E_{2g} symmetry [22]. A moderately intense peak was observed at lower Raman shift (413 cm^{-1}), this is attributed to octahedral 12k site metal oxide vibrational bonds due to E_{1g} symmetry [23]. Another weak Raman shift appears at 526 cm^{-1} corresponds to metal oxide vibrational bonds at octahedral 12k and 2a sites (mixed mode) due to E_{1g} symmetry[24]. Moreover, the same mixed mode metal oxide vibrational mode at octahedral 12k and 2a sites causes the occurrance of extremely weak mode at 465 cm^{-1}, this mode is assigned to A_{1g} symmetry[25]. The Fe-O bond stretching at octahedral ($4f_2$) site leads to the occurrance of active mode at 613 cm^{-1} due A_{1g} symmetry[25]. A vibrational mode at bipyramidal(2b) site give rise to an intense fassinating mode at 684 cm^{-1} due to A_{1g} symmetry. This differentiates the structure of hexagonal ferrite from the structure spinel ferrites[24]. Additionally, it was observed that the intensity of the peaks increased with increase Sr^{2+} ion concentration.

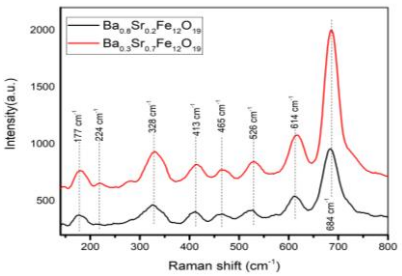

Figure 4. Raman shift of $Ba_{1-x}Sr_xFe_{12}O_{19}$ (x= 0.20, and 0.7)

Table 2. Raman mode of $Ba_{1-x}Sr_xFe_{12}O_{19}$ (x= 0.20, and 0.7)

Raman active mode (cm^{-1})	Symmetry	Mode assignment	Reference
177	E_{1g}	Whole spinel block	[21]
224	E_{1g}	Whole spinel block	[21]
292	A_{1g}	Octahedral (2a)	[22]
328	E_{2g}	Octahedral (12k)	[22]
413	E_{1g}	Octahedral (12k dominated)	[23]
465	A_{1g}	Octahedral (12k)	[25]
526	E_{1g}	Octahedral (12k and 2a)	[24]
613	A_{1g}	Octahedral ($4f_2$)	[25]
684	A_{1g}	Bipyramidal (2b)	[24]

Dielectric Analysis

Figures 5 and 6 show the frequency dependent dielectric constant and dielectric loss factor for $Ba_{1-x}Sr_xFe_{12}O_{19}$ (x= 0.20, and 0.7) respectively. İt was obseved that both the dielectric constant and dielectric loss factor decreases with increase in frequency up to intermediate frequency. The high values recorded at low frequencies could be as a result of existance of oxygen vacancies, interfacial dislocation, grain boundary defects, and large number of electron hopping between Fe^{3+} and Fe^{2+}. However, ε' high value observed at high frequencies are due to influence of high electrons hopping between Fe^{3+} and Fe^{2+} lagging prior to polarization relaxation. Therefore, any slight increase in ε' at high frequencies, causes the reduction of EM waves penetration depth due to the effect of increase in the skin effect. It was also observed that an increament in Sr^{2+} ions substitution, lead to a decreament in dielectric costant.

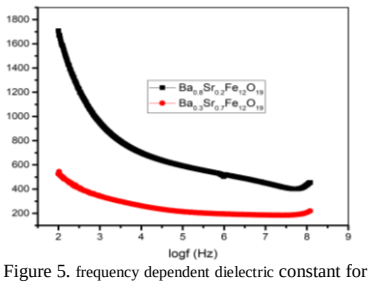

Figure 5. frequency dependent dielectric constant for $Ba_{1-x}Sr_xFe_{12}O_{19}$ (x= 0.20, and 0.7)

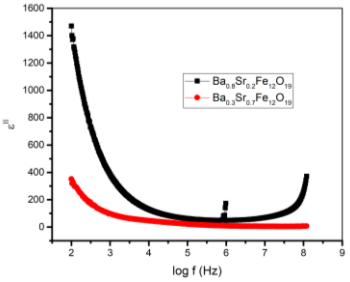

Figure 6. Frequency dependent dielectric loss factor for $Ba_{1-x}Sr_{0.2}Fe_{12}O_{19}$ (x= 0.20, and 0.7)

The dielectric loss ($tan\delta$) was used explain the nature of energy dissipated in dielectric system of hexagonal ferrite nanomaterials during the conduction of electrons. The variation of $tan\delta$ of $Ba_{1-x}Sr_xFe_{12}O_{19}$ (x= 0.20, and 0.7) with frequency at room temperature is shown in Figure 7. High $tan\delta$ was observed at low at high frequencies in all the samples, this shows the nature of energy loss in the materials. The grain boundaries's high resistivity at low frequencies prompted the need for high energy in for electron hopping to occur between Fe3+ and Fe2+ ions. Therefore, high $tan\delta$ or loss arises at low frequencies. The low resistivity of the material at intermediate frequencies arises due to conducting grains. Therefore, minimum energy is needed for electrons hopping to occur between Fe3+ and Fe2+ ions. Thus, the enegy loss in the material is very small at intermediate frequencies. Moreover, the calcination process give rise to defect dipoles due to exchange of Fe3+ ions to Fe2+ ions, this defect dipoles causes $tan\delta$ in $Ba_{0.8}Sr_{0.2}Fe_{12}O_{19}$ at higher frequencies. Sample $Ba_{0.8}Sr_{0.2}Fe_{12}O_{19}$ developed Resonance relaxation peaks at high frequencies, the observed behaviour arises in the process of transition between Fe3+ and Fe2+ ions when the frequency of applied electric field is equivalent to that of electrons jumping.

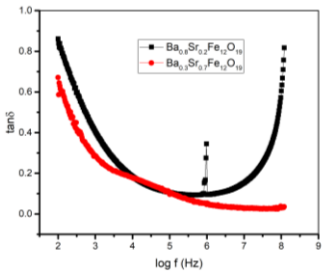

Figure 7 variation of $tan\delta$ of $Ba_{1-x}Sr_xFe_{12}O_{19}$ (x= 0.20, and 0.7) with frequency

The Cole-Cole plot, known as Nyquist plot, was used in order to study the nature of the grains and the resistance presented by the grain boundaries of the synthesized samples. This was done by studying the nature of the curve of the plot of imaginary part Z'' versus real part of Z' of the complex impedance Z^*. Figure 8 shows the nyquist plot of $Ba_{1-x}Sr_xFe_{12}O_{19}$ (x= 0.20, and 0.7) This plot were used in characterising non-Debye-like relaxation behaviour of the material, since it consists of semi-circlular arc begins at low frequency and end at high frequency. The semi-circlular part covering low frequencies shows the contributions due to grain boundary resistance (R_{gb}), meanwhile, the remaining semi-circlular part covering high frequencies signifies the contribution due to grain resistance (R_g) [21]. It was observed that there is no high frequency arc, Hence, it is concluded that grain resistance R_g has less or no contribution to dielectric properties of the samples. With these observations we can conclude that grain boundary resistance R_{gb} contribute immensily to the dielectric properties of material synthesized.

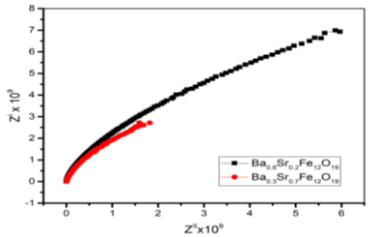

Figure 8. Nyquist plot of $Ba_{1-x}Sr_xFe_{12}O_{19}$ (x= 0.20, and 0.7)

The AC conductivity (σ_{ac}) of $Ba_{1-x}Sr_xFe_{12}O_{19}$ (x= 0.20, and 0.7) is presented in Figure 9. It is observed that from low upto intermediate frequencies that σ_{ac} shows frequency independent behaviour which occurs as a result of randomly distributed charge carriers, since grain boundaries are more active in reducing the frequency of electron hopping. At high frequencies, there was an instant hike in σ_{ac} of synthesized samples. The behaviour of σ_{ac} arises as a result of electron hopping between Fe^{3+} and Fe^{2+} ions at octahedral sites. That is the conductivity of the samples increases with increase in the frequency of applied field, as a result of increase in electron hopping between Fe^{3+} and Fe^{2+} ions at octahedral sites. It can be concluded that Sr^{+2}substitution enhances σ_{ac} at high frequencies.

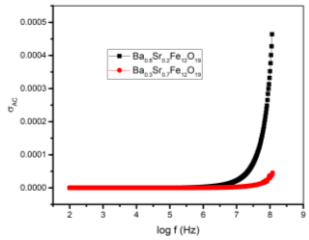

Figure 9. AC conductivity (σ_{ac}) of $Ba_{1-x}SrxFe_{12}O_{19}$ (x= 0.20, and 0.7)

The variation of $ln\sigma_{ac}$ with $ln\omega$ for $Ba_{1-x}Sr_xFe_{12}O_{19}$ (x= 0.20, and 0.7) is presented in figure 10. A linear relationship was observed between $ln\sigma_{ac}$ and $ln\omega$, that is to say there is a steady increase in $ln\sigma_{ac}$ with increase with increase in $ln\omega$. The calculated slope of this graph gives an exponential "s". With values between 0 and 1. when this value s = 0, a frequency independent conduction mechanism exist (i. e. DC conductivity), while for $s \leq 1$, it is dependent on frequency (i. e. AC conductivity) [25]. The calculated slope obtained from linear plot of $Ba_{0.8}Sr_{0.2}Fe_{12}O_{19}$ and $Ba_{0.3}Sr_{0.7}Fe_{12}O_{19}$, was found to be 0.8 and 0.7, respectively, Fig. 6f. Hence, It can be concluded that AC conductivity is the dominant conduction mechanism in the samples.

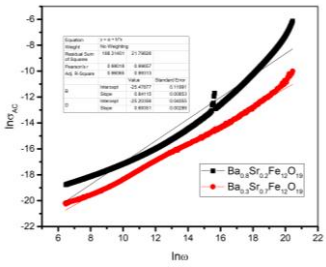

Figure 10. Variation of $ln\sigma_{ac}$ with $ln\omega$ for $Ba_{1-x}Sr_xFe_{12}O_{19}$ (x= 0.20, and 0.7)

Table 3: calculated electrical parameters from impedance analyser result using NOVA 1.11

SAMPLE CODE	R_e	R_g	C_g	R_{gb}	C_{gb}	σ_{AC}
$Ba_{0.8}Sr_{0.2}Fe_{12}O_{19}$	244	-3.70E+05	11.8pF	7.89E+07	6.64pF	2.17E-03
$Ba_{0.2}Sr_{0.7}Fe_{12}O_{19}$	47.7	4.59E+08	2.98pF	4.63E+06	3.32pF	4.54E-05

5.0 Conclusıon

M-type Barium nanohexaferrites with $Ba_{1-x}Sr_xFe_{12}O_{19}$ (x= 0.20, and 0.7) chemical compositions were succesfully syntesized. The formation of single phase hexagonal ferrites was confirmed from XRD analysis, it also reveal the presence of hematide in sample $Ba_{0.8}Sr_{0.2}Fe_{12}O_{19}$ and the cystallites sizes were in the range of 26.40nm-29.91nm, the lattice constants were found to decrease with increase in ions substitutions. The FTIR spectra of the sample show three dominants peaks in the range 400-600 cm^{-1} which indicate the formation of the desired hexaferrites structure. The FESEM micrographs revealed large crystallites with shapes close to the hexagonal platelet-like shapes, whose size are non uniformly distributed, with highest degree of agglomaration due to magnetic interactions between the crystallites. The dielectric properties were studied using impedance measurements obtained in the frequency range 100Hz-120MHz. The dielectric constant, dielectric loss and conductivity were analysed using Maxwell-Wagner model. Dielectric constant was enhanced at high frequency in the entire sample and reduction of dielectric loss is also observed with further ions substitutions. The grain boundary resistance contributes the most to the dielectric properties as indicated by Nyquist plot, whereas the Ac conductivity is the dominant conducting mechanism in the material which was found to decrease with increase in ions substitutions.

Reference

[1] Akaiwa, Y., & Okazaki, T. (1974). Applıcatıon of a hexagonal ferrıte to a mıllımeter-wave ycırculator. Ieee Transactions on Magnetics, MA10(2), 374-378. doi:10.1109/tmag.1974.1058336

[2] R. C. Pullar, "Hexagonal ferrites: A review of the synthesis, properties and applications of hexaferrite ceramics," *Prog. Mater. Sci.*, vol. 57, no. 7, pp. 1191–1334, 2012.

[3] R. C. Pullar, I. K. Bdikin, and A. K. Bhattacharya, "Magnetic properties of randomly oriented BaM , SrM , Co 2 Y , Co 2 Z and Co 2 W hexagonal ferrite fibres," *J. Eur. Ceram. Soc.*, vol. 32, pp. 905–913, 2012.

[4] Li, J., Zhang, H. W., Liu, Y. N., Liao, Y. L., Ma, G. K., & Yang, H. (2015). Co-Ti cosubstitution of M-type hexagonal barium ferrite. Materials Research Express, 2(4). doi:10.1088/2053-1591/2/4/046104

[5] Shipko, M. N., Kostishin, V. G., Stepovich, M. A., & Korovushkin, V. V. (2017). Modifying the Properties of Ferrite Materials with a Hexagonal Structure via Treatment in Corona Discharge Plasma. Journal of Surface Investigation, 11(1), 142-145. doi:10.1134/s1027451016050803

[6] Liu, J. L., Yang, M., Wang, S. Y., Lv, J. Q., Li, Y. Q., & Zhang, M. (2018). Sol-gel autocombustion synthesis and properties of Co(2)Z-type hexagonal ferrite ultrafine powders. Journal of Magnetism and Magnetic Materials, 454, 1-5. doi:10.1016/j.jmmm.2018.01.049

[7] Malik, H., Khan, M. A., Hussain, A., Warsi, M. F., Mahmood, A., & Ramay, S. M. (2018). Structural, spectral, thermal and dielectric properties of Nd-Ni co-doped SrBa-Cu hexagonal ferrites synthesized via sol-gel auto-combustion route. Ceramics International, 44(1), 605-612. doi:10.1016/j.ceramint.2017.09.219

[8] Singh, C., Bai, Y., Narang, S. B., Mishra, S. R., Singh, D., Sombra, A. S. B., . . . Kagdi, A. (2019). Bandstop Passive Filter Characteristics of Hexagonal Ferrite Composites at XBand. Journal of Electronic Materials, 48(10), 6189-6193. doi:10.1007/s11664-01907424-y

[9] Takabayashi, H., Kato, Y., Kagotani, T., Book, D., Sugimoto, S., Homma, M., . . . Houjou, Y. (2000). Effect of crystal orientation on the magnetic resonance properties of M-type hexagonal ferrites. Materials Transactions Jim, 41(9), 1184-1187. doi:10.2320/matertrans1989.41.1184

[10] Yasmin, N., Abdulsatar, S., Hashim, M., Zahid, M., Gillani, S. F., Kalsoom, A., . . . Mirza, M. (2019). Structural and magnetic studies of Ce-Mn doped M-type SrFe12O19 hexagonal ferrites by sol-gel auto-combustion method. Journal of Magnetism and Magnetic Materials, 473, 464-469. doi:10.1016/j.jmmm.2018.10.076

[11] Zhang, Y., Wang, H. T., Liu, J. W., Yan, S. H., & Shen, J. F. (2007). Preparation and electromagnetic properties of lanthanum hexagonal ferrite Ba0.8La0.2(Zn0.5Ni0.5)(2x)CoxFe15O27. Rare Metal Materials and Engineering, 36, 308-311. Retrieved from <Go to ISI>://WOS:000252181200071

[12] Mohammed, J., Tchouank Tekou Carol T., Basandrai, D., Gopala R., Bhadu, S., Kumar, Narang, S. B., Srivastava A. K.(2019) "Design of nano-sized ¬ Pr3+–Co2+ substituted M-type strontium hexaferrites for optical sensing and electromagnetic interference (EMI) shielding in ¬ K u band," Appl. Phys. A, 125, 251 https://doi.org/10.1007/s00339-019-2545-5

[13] Mohammed, J., Hafeez, H. Y., Tchouank Tekou Carol T., Ndikilar, C. E., Sharma, J., Pradip K. Maji, Sachin K. Godara, Srivastava, A. K., (2019) "Structural, dielectric, and magneto-optical properties ofCu2+-Er3+ substituted nanocrystalline strontium hexaferrite," Mater. Res. Express, 6(5), 056111 https://doi.org/10.1088/2053-1591/ab063b

[14] Mohammed, J., Suleiman, A. B., Hafeez, H. Y., Tchouank Tekou Carol T., J. Sharma, Gopala R. Bhadu, Sachin K. Godara, Srivastava, A. K., (2018) "Effect of heat-treatment on the magnetic and optical properties of Sr0.7Al0.3Fe11.4Mn0.6O19," Mater. Res. Express, 5(8), 086106 https://doi.org/10.1088/2053-1591/aad1e5

[15] Ashima, H, Sujada, S; Ashish, A; Reetu, D. (2015): Crystal Structure Refinement, Dielectric and magnetic materials of Ca/Pb substituted $SrFe_{12}O_{19}$ Hexaferrites. Journal of Magnetism and Magnetic Materials. 378, 46-52: http: //doi.org/10.1016/j.jmmm.2015.03.078

[16] Rafiq, M. A., Waqar, M., Mirza, T. A., Farooq, A., & Zulfiqar, A. (2017). Effect of Ni2+ Substitution on the Structural, Magnetic, and Dielectric Properties of Barium Hexagonal Ferrites (BaFe12O19). Journal of Electronic Materials, 46(1), 241-246. doi:10.1007/s11664-016-4872-z

[17] Vadivelan, S., Victor Jaya, N. (2016) "Investigation of magnetic and structural properties of copper substituted barium ferrite powder particles via co-precipitation method," Results in physics 6, 843-850 https://doi.org/10.1016/j.rinp.2016.07.013

[18] Mosleh, Z., Kameli, P., Poorbaferani, A., Ranjbar, M., Salamati, H. (2016) "Structural, magnetic and microwave absorption properties of Ce-doped barium hexaferrite," J. Magn. Magn. Mater., 397, 101–107 https://doi.org/10.1016/j.jmmm.2015.08.078

[19] Sun Chang, Sun Kangning, Chui Pengfei. (2012) "Microwave absorption properties of Ce-substituted M-type barium ferrite," J. Magn. Magn. Mater., 324, 802–805 https://doi.org/10.1016/j.jmmm.2011.09.023

[20] Pullar, R. C., & Bhattacharya, A. K. (2001). The synthesis and characterization of the hexagonal Z ferrite, Sr3Co2Fe24O41, from a sol-gel precursor. Materials Research Bulletin, 36(78), 1531-1538. doi:10.1016/s0025-5408(01)00596-7

[21] Tchouank Tekou Carol T., J. Mohammed, B. H. Bhat, S. Mishra, S. K. Godara, A. K. Srivastava.(2019) "Effect of Cr-Bi Substitution on the structural, electrical and magnetic properties of strontium hexaferrites," Physica B: Condensed Matter, 411681. https://doi.org/10.1016/j.physb.2019.411681

[22] Kumar, S., Supriya, S., Pandey, R., Pradhan, L. K., Singh, R. K., Kar, M. (2018) "Effect of lattice strain on structural and magnetic properties of Ca substituted barium hexaferrite," J. Magn. Magn. Mater., 458, 30–38 https://doi.org/10.1016/j.jmmm.2018.02.093

[23] Kumar, S., Supriya, S., Kar. M. (2017) "Effect of Sintering Temperature on Electrical Properties of BHF Ceramics Prepared by Modified Sol-Gel Method," Mater. Today Proc., 4(4), 5517–5524 https://doi.org/10.1016/j.matpr.2017.06.007

[24] Rana, K., Thakur, P., Tomar, M., Gupta, V. Thakur, A. (2018) "Investigation of cobalt substituted M-type barium ferrite synthesized via co- precipitation method for radar absorbing material in Ku-band (12–18 GHz)," Ceram. Int., 44, 6370–6375 https://doi.org/10.1016/j.ceramint.2018.01.028

[25] Mohammed, J., Hafeez, H. Y., Carol, T. T. T., Sharma, J., Isma'il, U. T., Godara, S. K., & Srivastava, A. K. (2019). Structural, dielectric and magnetic properties of Al-Mn substituted nano-sized M-type strontium hexagonal ferrites. Materials TodayProceedings, 18, 533-541. doi:10.1016/j.matpr.2019.06.392